nature physics

Article

https://doi.org/10.1038/s41567-024-02653-3

Strain tuning of vestigial three-state Potts nematicity in a correlated antiferromagnet

Received: 30 May 2023

Accepted: 27 August 2024

Kyle Hwangbo[1,5], Elliott Rosenberg[1,5], John Cenker[1], Qianni Jiang[1], Haidan Wen[2], Di Xiao[1,3,4], Jiun-Haw Chu[1] ✉ & Xiaodong Xu[1,3] ✉

Electronic nematicity is a state of matter in which rotational symmetry is spontaneously broken and translational symmetry is preserved. In strongly correlated materials, nematicity often emerges from fluctuations of a multicomponent primary order, such as spin or charge density waves, and is termed vestigial nematicity. One widely studied example is Ising nematicity, which arises as a vestigial order of collinear antiferromagnetism in the tetragonal iron pnictide superconductors. Because nematic directors in crystals are restricted by the underlying crystal symmetry, recently identified quantum materials with three-fold rotational symmetry offer a new platform to investigate nematic order with three-state Potts character. Here we demonstrate strain control of three-state Potts nematicity as a vestigial order of zigzag antiferromagnetism in $FePSe_3$. Optical linear dichroism measurements reveal the nematic state and demonstrate the rotation of the nematic director by uniaxial strain. We show that the nature of the nematic phase transition can also be controlled by strain, inducing a smooth crossover transition between a Potts nematic transition and an Ising nematic flop transition. Elastocaloric measurements demonstrate the signatures of two coupled phase transitions, indicating that the vestigial nematic transition is separated from the antiferromagnetic transition. This establishes $FePSe_3$ as a system to explore three-state Potts vestigial nematicity.

Electronic nematicity has drawn interest over the years due to its intertwined relationship with many strongly correlated phases. The importance of nematic order was highlighted in tetragonal iron pnictide superconductors, where speculation continues that the fluctuations of the symmetry-breaking phase could be the driving pairing mechanism[1–3]. Recently, there have been an increasing number of reports regarding the nematic order in quantum materials with rich phase diagrams, such as twisted graphene systems[4–7] and kagome lattice superconductors[8–11], further hinting at the important role of nematicity. However, in contrast to the widely studied Ising nematicity ($\mathbb{Z}_2$) in tetragonal iron pnictides, the nematic order in these recent systems of interest is frequently represented by a three-state Potts model ($\mathbb{Z}_3$), reflecting their C_3 and C_6 rotational crystal symmetries. Understanding the behaviour of three-state Potts nematicity is critical in untangling its complex interplay with other strongly correlated phases.

Three-state Potts nematic order has been theorized to have properties that are distinct from Ising nematicity[12]. Although anisotropic strain always smears out an Ising nematic transition and turns it into a crossover transition, a three-state Potts nematic transition can be switched to either a crossover transition or an Ising nematic flop transition, depending on the sign of strain. Previous experimental investigations of three-state Potts nematic order only investigated the reorientation of nematic domains with static strain well below the transition temperature[13,14], but the effect of strain near and above the phase transition has not been explored. Here we use optical linear dichroism (LD) and elastocaloric (EC) measurements in conjunction

---

[1]Department of Physics, University of Washington, Seattle, WA, USA. [2]Advanced Photon Source, Argonne National Laboratory, Lemont, IL, USA. [3]Department of Materials Science and Engineering, University of Washington, Seattle, WA, USA. [4]Pacific Northwest National Laboratory, Richland, WA, USA. [5]These authors contributed equally: Kyle Hwangbo, Elliott Rosenberg. ✉e-mail: jhchu@uw.edu; xuxd@uw.edu

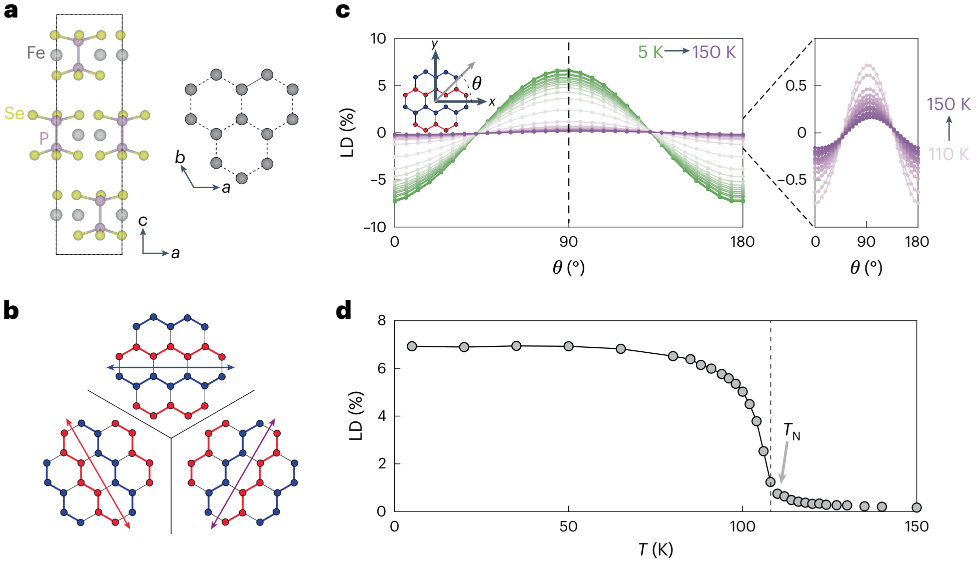

Fig. 1 | Zigzag AFM order and three-state degeneracy. a, Crystal structure of $FePSe_3$. The Fe atoms form a honeycomb lattice when viewed in the *a*–*b* plane. **b**, Three possible choices of the zigzag spin chain directions on a honeycomb lattice. The arrows represent the nematic director corresponding to each choice of the zigzag AFM order. **c**, Optical LD response of a thin bulk $FePSe_3$ flake as the polarization angle of the incident light (θ) is rotated with respect to the zigzag spin chain direction at various temperatures. The right panel is the zoomed-in view of the polarization-dependent LD signal at temperatures above T_N. **d**, LD response as a function of temperature when the incident polarization is orthogonal to the zigzag spin chains (polarization angle indicated by the grey dashed line in **c**). The dashed line indicates T_N.

with in situ, tunable uniaxial strain—the conjugate field to nematicity—to probe and control the three-state Potts nematicity as a vestigial order of the zigzag antiferromagnetic (AFM) phase in a van der Waals layered material—$FePSe_3$. The optical LD enables direct probing of the nematic order parameter, and the EC effect (ECE) measures the change in entropy induced by strain and is sensitive to the thermodynamic anomalies associated with phase transitions. The combination of these two techniques is of central importance for determining if $FePSe_3$ indeed exhibits vestigial three-state Potts nematicity.

The material of interest, $FePSe_3$, belongs to a family of transition metal phosphorous trichalcogenide antiferromagnets (MPX_3, M = Fe, Mn, Ni; X = S, Se). In particular, $FePSe_3$ is a zigzag antiferromagnet with a Néel temperature (T_N) of ~108 K (refs. 15–17). The magnetic moments point in the out-of-plane direction and mostly localize around the Fe atoms, which form a honeycomb lattice with C_3 symmetry (Fig. 1a). This leads to three possible arrangements of the zigzag spin chains on the honeycomb structure (Fig. 1b). As discussed in previous work, this type of AFM order can exhibit nematic degrees of freedom in which the bonds corresponding to the direction of the AFM wavevector elongate or shrink, breaking the rotational symmetry of the honeycomb lattice[13]. A vestigial nematic phase may condense at temperatures above the AFM phase transition, analogous to the Ising nematicity observed in pnictide superconductors at temperatures above the collinear AFM order[13,18,19]. Thus, the signatures of the three-state Potts nematic order for this system can manifest in a separate phase transition at temperatures above the AFM phase transition, as well as a clear asymmetry of material properties for tensile and compressive strains along a given direction, in contrast to Ising nematicity[13].

We first discuss LD measurements in which the anisotropy of the optical conductivity serves as a proxy for the nematic order parameter. We performed a phase-modulation-based optical LD measurement on a thin bulk flake (~30 nm) that was exfoliated on a SiO_2/Si substrate. Figure 1c shows the measured LD as a function of the polarization angle (θ) of incident light at different temperatures. The photon energy is chosen to be 1.95 eV as it gives rise to a large LD signal (Extended Data Fig. 1). The measured LD follows a cos(2θ) dependence below T_N, which is expected if one AFM wavevector is dominant. The dependence of polarization angle allows us to determine the direction of the zigzag spin chain. The most negative (maximum) value of LD corresponds to the incident light polarization parallel (orthogonal) to the zigzag spin chain[20]. This LD measurement is similar to previous studies on $NiPS_3$ and $FePS_3$, where the concomitant rise of a strong LD signal with the onset of the zigzag AFM order was used as a proxy measure of the zigzag AFM order[20–22]. Nevertheless, unlike the magnetic order parameter that breaks the time-reversal symmetry, the LD signal probes rotational symmetry breaking, which is even under time reversal. This implies that the LD signal is proportional to the quadratic terms of zigzag AFM order parameter, which can be non-zero due to AFM fluctuations even in the absence of long-range magnetic order. Note that optical anisotropy is absent in Mn compounds of the family[20], which exhibit Néel-type spin textures. Thus, previous studies of the AFM order in Mn compounds have instead relied on second-harmonic generation measurements[23–25].

Figure 1d presents the temperature dependence of the maximum LD signal, which follows a trend resembling that of an order parameter for a second-order phase transition. However, unlike a magnetic order parameter that should completely disappear above T_N, there is a persistent LD signal at temperatures substantially above T_N, forming a tail-like feature. Furthermore, polarization-dependent LD measurements from 110 K to 150 K (Fig. 1c) clearly demonstrate the surviving cos(2θ) dependence above T_N. This peculiar behaviour has been previously observed in ionic crystal systems such as NiO (ref. 26) and dubbed the fluctuation tail in the literature[27,28]. In $FePSe_3$, the zigzag AFM order vanishes above T_N, accompanying strong spin fluctuations. Because LD has the same symmetry as a nematic order parameter, that is, changing sign under 90° rotation, the observed residual LD signal suggests that there is a finite nematic order parameter far above T_N. As discussed above, the nematic order is a vestigial order formed by the fluctuations of zigzag AFM order. The tail-like nature of the signal probably arises from a symmetry-breaking strain that couples with the system's diverging nematic susceptibility towards T_N, indicative of a nematic instability in $FePSe_3$.

Similar fluctuation tails in the LD temperature dependence have been observed previously in $FePS_3$ and $NiPS_3$ (refs. 20–22), but it is important to note that the sulfide compounds have a $C2/m$ monoclinic

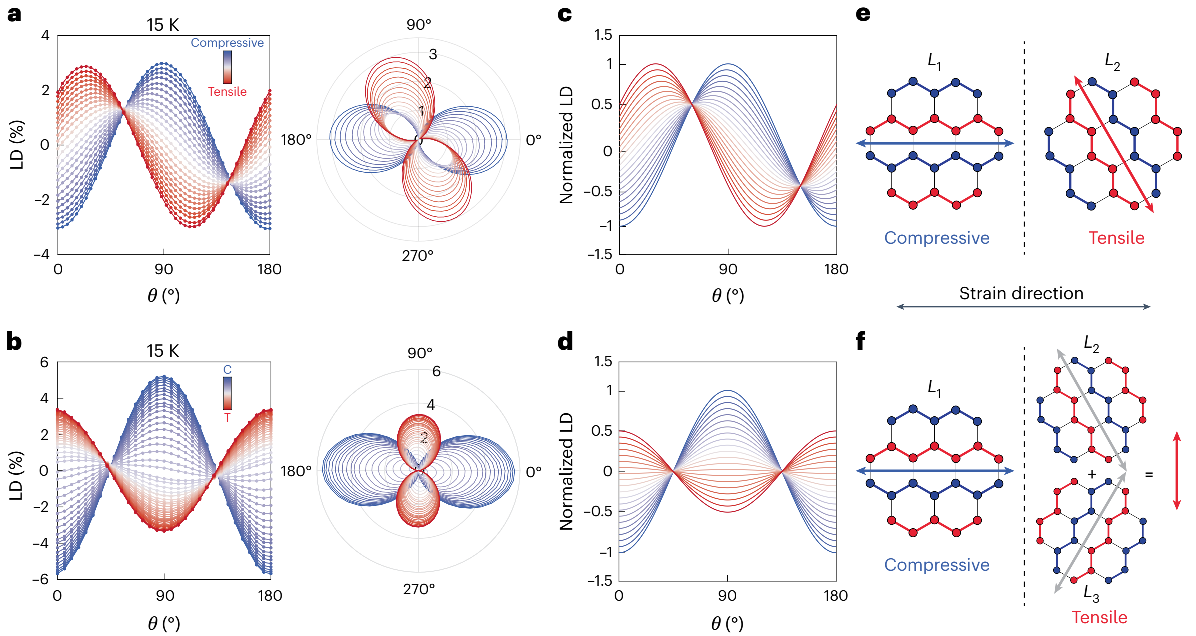

Fig. 2 | Strain control of zigzag AFM order at 15 K. **a**, Polarization-dependent LD response as strain is applied for the first thermal cycle. The polar graphs track the rotation of the nematic director as strain is applied. **b**, Polarization-dependent LD response as strain is applied for the second thermal cycle, after the sample was remounted onto the strainer. **c**, Simulated LD response of nematic domain population model with two nematic domains (see the main text for details). **d**, Simulated LD response of nematic domain population model with three nematic domains. **e**, Illustration of the zigzag AFM order at the maximum compressive and tensile strains applied for the sample response presented in **a**. The arrows represent the nematic director at the respective strain states. **f**, Illustration of the zigzag AFM order presented at the maximum strain points for the sample response presented in **b**. For the tensile response, there are coexisting zigzag AFM domains in which the vector summation of the domains' nematic directors (grey arrows) result in an overall nematic director (red arrow) that is vertical (orthogonal to the nematic director of compressive strain).

structure. Therefore, the monoclinic tilt acts as the symmetry-breaking mechanism, which creates a preferential direction for the zigzag spin chain. By contrast, $FePSe_3$ belongs to the $R3$ space group and reportedly lacks a monoclinic distortion (Fig. 1a)[29]. Consequently, the three orientations of the zigzag spin chains should be energetically degenerate and the fluctuations of the nematic order between the three states should average out above T_N, leading to an isotropic optical response and the absence of the fluctuation tail. As the sample is cooled below T_N, the zigzag order should then stochastically select one of the three possible spin chain directions, leading to an archetypal first-order Potts nematic transition[13]. However, the zigzag AFM direction (that is, the maximum LD direction) and the observed fluctuation tail are robust against various thermal cycles, implying the presence of a certain symmetry-breaking mechanism that lifts the degeneracy. This is most probably due to the small strains introduced during the exfoliation of flakes onto the SiO_2/Si wafer.

To gain further insight into the nematic order of $FePSe_3$, we utilized a homebuilt cryo-strain device capable of applying in situ strain to two-dimensional materials[30] (Methods). The $FePSe_3$ flake was carefully aligned so that the crystal zigzag axis was parallel to the strain direction (Extended Data Fig. 2). We use the silicon Raman mode to calibrate the applied strain (Methods and Extended Data Fig. 3). The polarization-angle-dependent LD signal was then measured as a function of applied strain at the base temperature (15 K) (Fig. 2a, left). Remarkably, the LD signal underwent a dramatic evolution as the strain is swept from compressive to tensile. The corresponding polar plot (Fig. 2a, right) tracks the rotation of the nematic director, which was inferred from the polarization-dependent LD response, as strain was applied. When comparing the LD response at the two extremes of the compressive- and tensile-strain regimes, we found that the nematic director is separated exactly by 2π/3 and the LD strengths remained comparable.

Figure 2b presents the measurements conducted on the same sample as that in Fig. 2a, but for a different thermal cycle after the sample was remounted. The LD signal exhibits a strikingly different behaviour. As shown in the polar plot, by varying the strain from being compressive to tensile, the lobe along the horizontal axis slowly shrinks, vanishes and then grows along the orthogonal direction. There is an effective π/2 rotation in the nematic director between the two end points of the compressive- and tensile-strain regimes. The LD strength is also distinctly less under tensile strain than under compressive strain.

To understand the underlying mechanism, we modelled the strain-controlled population of the $\mathbb{Z}_3$ nematic domains based on two different premises. We hypothesized that the domains are determined not only from the estimated induced strain but also from its vertical relaxation. This hypothesis was supported by our spatial LD mapping as a function of strain (Extended Data Fig. 4). The observation presented in Fig. 2a can be reproduced by the superposition of the LD signals of two nematic domains with angles along 0 and 2π/3 (Fig. 2e). Figure 2c plots the simulated overall LD signal as the relative weight of the two domains is varied by strain (Methods provides the simulation details). The excellent agreement between the simulation and observation (Fig. 2a) supports our strain-controlled nematic domain population model.

To explain the trend observed in Fig. 2b, we included the third nematic domain with an angle of −2π/3 in the domain population model. As shown by the schematic in Fig. 2f, in this situation, the nematic domains of 2π/3 and −2π/3 are degenerate and equally populated as tensile strain is applied. In this case, the nematic director seems to rotate by π/2 because the vector summation of the nematic directors result in an overall vector that points orthogonally to the nematic director of the compressive side. Similarly, using this domain population model, we accurately obtain the trend (Fig. 2d) that was observed in Fig. 2b. The distinct behaviour between the two thermal

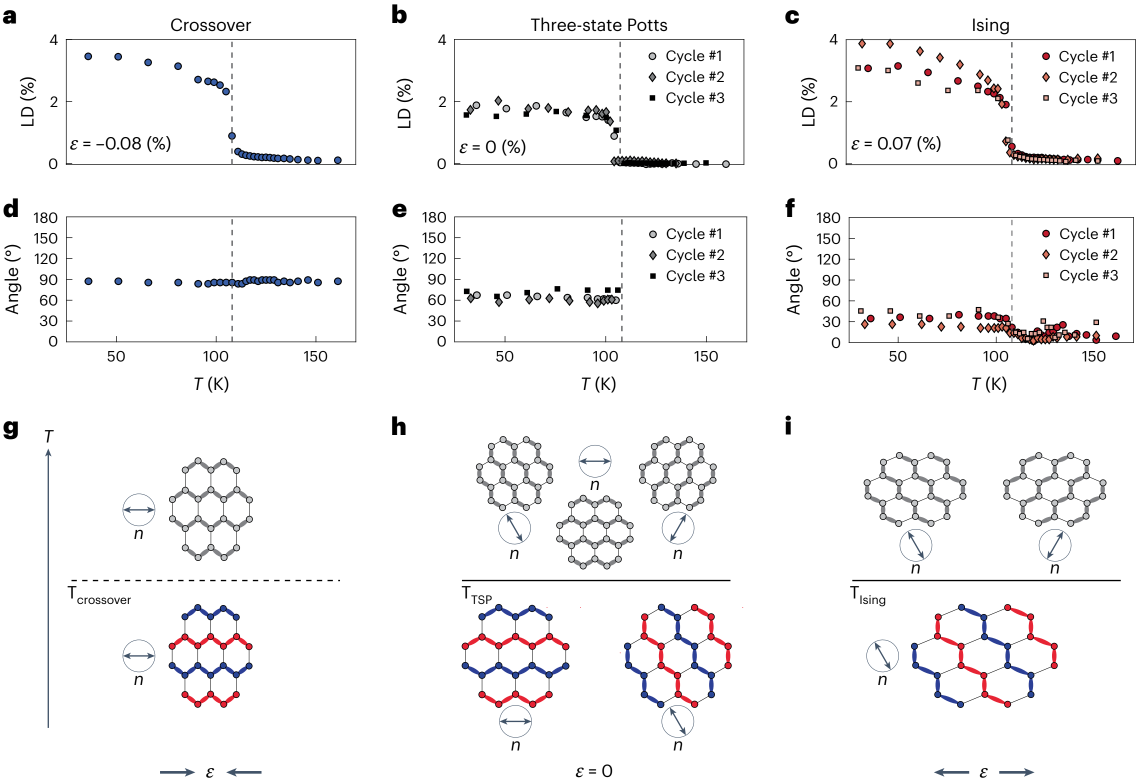

Fig. 3 | Temperature dependence of LD under different strains. **a**–**c**, LD response as a function of temperature for compressive strain (**a**), zero strain (**b**) and tensile strain (**c**). The incident polarization angle was orthogonal to the nematic director. The dashed line marks the magnetic transition temperature (~108 K). The responses for three different thermal cycles for the same sample are shown in **b** and **c**. **d**, Evolution of the nematic director as a function of temperature for compressive strain. The angles are offset by 90° at each temperature point for **d**–**f**. **e**, Evolution of the nematic director as a function of temperature for near-zero strain. Points above the transition temperature are omitted for **e** due to the lack of LD response. **f**, Evolution of the nematic director as a function of temperature for tensile strain. **g**–**i**, Illustration of the nematic order as the temperature is lowered with compressive strain (**g**), zero strain (**h**) and tensile strain (**i**). The thicker, grey bonds highlight the direction of the nematic order. The crossover transition ($T_{crossover}$) observed in **a** and **d** is shown in **g**, and the three-state Potts transition (T_{TSP}) presented in **b** and **e** is shown in **h**. The Ising transition (T_{Ising}) in **c** and **f** is shown in **i**.

cycles probably resulted from subtle misalignments of the sample with respect to the piezo-stack poling axis, introduced during remounting of the sample onto the strainer apparatus for each thermal cycle. When the sample and the piezo-stack poling axis are nearly perfectly aligned, both 2π/3 and −2π/3 domains are favoured under tensile strain (Fig. 2b). However, when there is a small misalignment between the substrate and the piezo-stack poling axis, one of the domains is favoured and pinned (Fig. 2a).

The seamless agreement between the observed strain responses below T_N and the domain population model demonstrates that strain can be used to control the orientation of the AFM zigzag spin chains. We corroborate our results further by conducting polarization-resolved Raman spectroscopy on a sample that exhibited the 2π/3 shift of the nematic director (Extended Data Figs. 5 and 6). Note that strain-induced, nematic domain repopulation was also observed in $Fe_{1/3}NbS_2$, which is a three-state Potts system but with a triangular crystal lattice[13].

We then examined the effects of strain on the putative fluctuation tail above T_N for the thermal cycle presented in Fig. 2a. This part of the study was conducted by performing a strain sweep from compressive to tensile as the sample was warmed from the base temperature. The phonon mode of the silicon substrate was used to convert the piezoelectric voltage to applied strain for each temperature (Methods). Figure 3a shows the temperature dependence of LD at −0.08% strain, where the fluctuation tail clearly remains. As described above, for compressive strain, there is a delineated direction for which the nematic order will form due to strain-induced anisotropy. Thus, rather than having a distinct phase transition, there is a crossover behaviour at T_N (Fig. 3g). This transition is similar to the smeared nematic transitions that have been observed previously in iron pnictides. By contrast, Fig. 3b shows the temperature-dependent LD at zero strain, where the fluctuation tail nearly vanishes, and the LD sharply onsets at T_N. These results confirm that the fluctuation tail observed earlier in the as-exfoliated crystal is a product of strain-induced nematicity in the system and indicates a large nematic susceptibility in $FePSe_3$.

The effect of strain on the phase transition character was further examined by tracking the nematic director and examining the incident polarization angle at which the LD response reaches its maximum as a function of strain. Figure 3d shows the angle of the maximum polarization as a function of temperature for −0.08% strain. Because the formation direction of the nematic order is fixed along the strain direction, there are no changes to the polarization angle as the sample is cooled below the transition temperature, providing additional evidence of the crossover behaviour. Figure 3e shows the same plot for the zero-strain response. Below the transition temperature, where we observe a finite LD response, the nematic director is separated by 30° with respect to its compressive strain counterpart. This suggests that there is an equal population of two nematic domains below the transition temperature. As the strain was swept from compressive to tensile, we hypothesize that the layers of the $FePSe_3$ flake that are closer to the substrate favour the tensile nematic states, whereas the layers near the vacuum interface favour the compressive nematic state, as a result of the vertical strain relaxation discussed earlier. Figure 3h illustrates the orientations of the nematic states under nominal zero

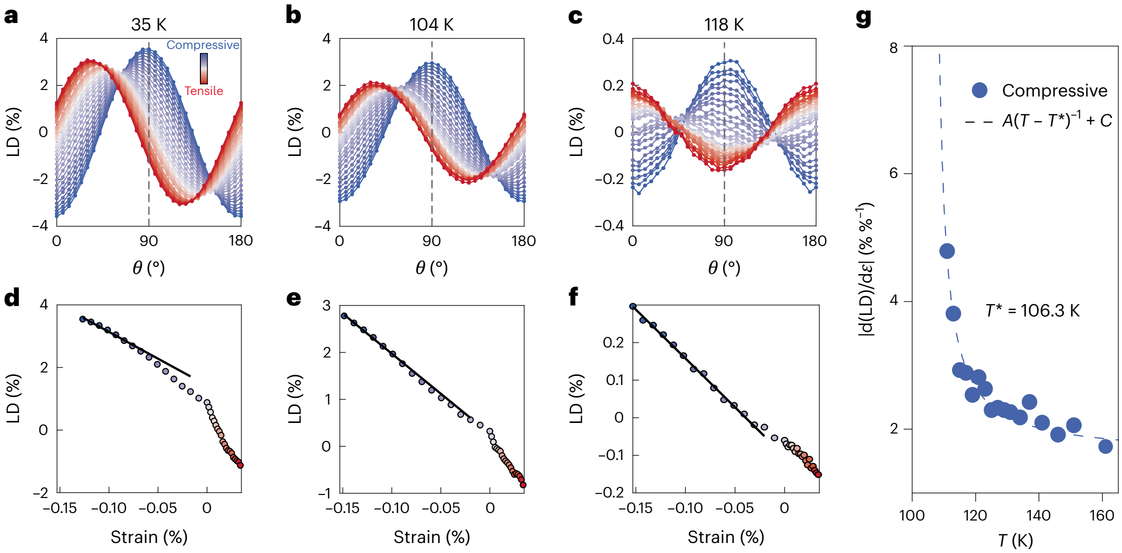

Fig. 4 | Nematic susceptibility of the compressive side. a–c, Polarization-dependent LD response as a function of strain at 35 K (**a**), 104 K (**b**) and 118 K (**c**). **d–f**, LD values at a fixed polarization angle, indicated by the dashed lines in **a–c** as strain is applied for 35 K (**d**), 104 K (**e**) and 118 K (**f**). The black line exemplifies the linear fitting that was performed for the compressive side to extract the rate of change in LD strength versus strain at different temperature points. **g**, Temperature dependence of the nematic susceptibility obtained by d(LD)/dε in the compressive-strain regime. The dashed line describes a Curie–Weiss fit to the data above the nematic phase transition.

strain. The existence of unavoidable built-in strain also implies that a true three-state Potts transition that only exists in the zero-strain limit is difficult to reach in this experimental condition.

Figure 3f shows the temperature-dependent polarization angle when sufficient tensile strain (0.07%) is applied to shift the zigzag direction at the base temperature and to partially lift the degeneracy above the transition temperature. Under tensile strain, the formation of the nematic order along the strain direction is precluded. Above the transition temperature, there are only fluctuations between the two possible nematic states. These fluctuations also result in a finite, anisotropic response (Fig. 3c,f) that is orthogonal to the compressive strain response, akin to the behaviour at base temperature (Fig. 2f). As the sample approaches the transition temperature, it undergoes an Ising-like phase transition, making a choice between the two possible nematic directions and forming a nematic order that is rotated 120° from the nematic state driven by compressive strain. Thus, there is a 30° shift in the nematic director as the sample is cooled below the transition temperature. The sample starts with a nematic director orthogonal to that of the compressive state above the transition temperature and forms a nematic director that is rotationally separated 120° from the compressive state below the transition (Fig. 3i). In particular, this behaviour is unique to three-state Potts systems[12,18] in which the nature of the phase transition is qualitatively different between the tensile and compressive strain states, as shown by our experimental results.

The coupling between nematic order and anisotropic strain of the same symmetry enables us to investigate the nematic susceptibility using the LD response induced by anisotropic compressive strain. The rate of change in LD with respect to strain, that is, d(LD)/dε, is proportional to the nematic susceptibility above the phase transition. Figure 4 shows the strain- and polarization-dependent LD responses, at select temperature points, with a distinct response in the compressive side. Extracting the LD value by fixing the polarization orthogonal to the nematic director, we observe that the nematic order couples linearly to the applied strain (Fig. 4d–f). By the linear fitting of LD versus ε in the compressive-strain range for all the temperature points, we obtain the d(LD)/dε curve (Fig. 4g). Analogous to the observations in Ising nematic systems[31], we observe a divergent behaviour of the nematic susceptibility, characterized by a Curie–Weiss-like form, with a Weiss temperature slightly below the phase transition temperature, as we cool towards the transition temperature.

Although we can extract the nematic susceptibility in the large-compressive-strain range, linear fitting becomes less reliable near-zero strain due to the small LD signal after background subtraction. Another issue is whether the nematic transition is separated from the AFM transition, which we have assumed to occur at the same temperature up to this point. To address these issues, we measured the ECE of FePSe$_3$. EC measurements[32,33] probe the strain derivatives of the entropy by inducing a perturbative a.c. strain in the sample and measuring the corresponding temperature changes in quasi-adiabatic conditions. For systems featuring Ising nematic phases that couple bilinearly to strain, the amplitude of the relevant ECE will be proportional to the d.c. strain multiplied by the temperature derivative of the nematic susceptibility for temperatures above the phase transition:

$$\frac{\mathrm{d}T}{\mathrm{d}\varepsilon} = -\frac{T\lambda^2\varepsilon_0}{C_\varepsilon}\frac{\mathrm{d}\chi}{\mathrm{d}T},$$

where λ is the nemato-elastic coupling, C_ε is the heat capacity of the sample, ε_0 is the offset d.c. strain experienced by the sample and $\chi \propto \frac{1}{T-T^*}$ is the nematic susceptibility for an Ising nematic[32,33].

As discussed in Supplementary Information, both nematic susceptibility and ECE are identical for three-state Potts nematicity but only in the zero-strain limit, more specifically having first-order corrections of $\frac{\varepsilon}{a_0^2(T-T^*)^2}$ that differentiate the compressive- and tensile-strain regimes. At temperatures closer to the phase transition, these corrections will become more prominent. The extracted d.c. strain derivative of the ECE will have a more complex relationship with the nematic susceptibility, including an asymmetry between the tensile- and compressive-strain regimes. Nonetheless, the ECE serves as an informative proxy for the susceptibility of the vestigial nematic order parameter at temperatures above the phase transitions with respect to the strain it couples to, which is the antisymmetric E$_{2g}$ strain ($\varepsilon_{xx} - \varepsilon_{yy}$).

When strain tensor elements are induced which do not bilinearly couple to the order parameter but instead tune the phase transition

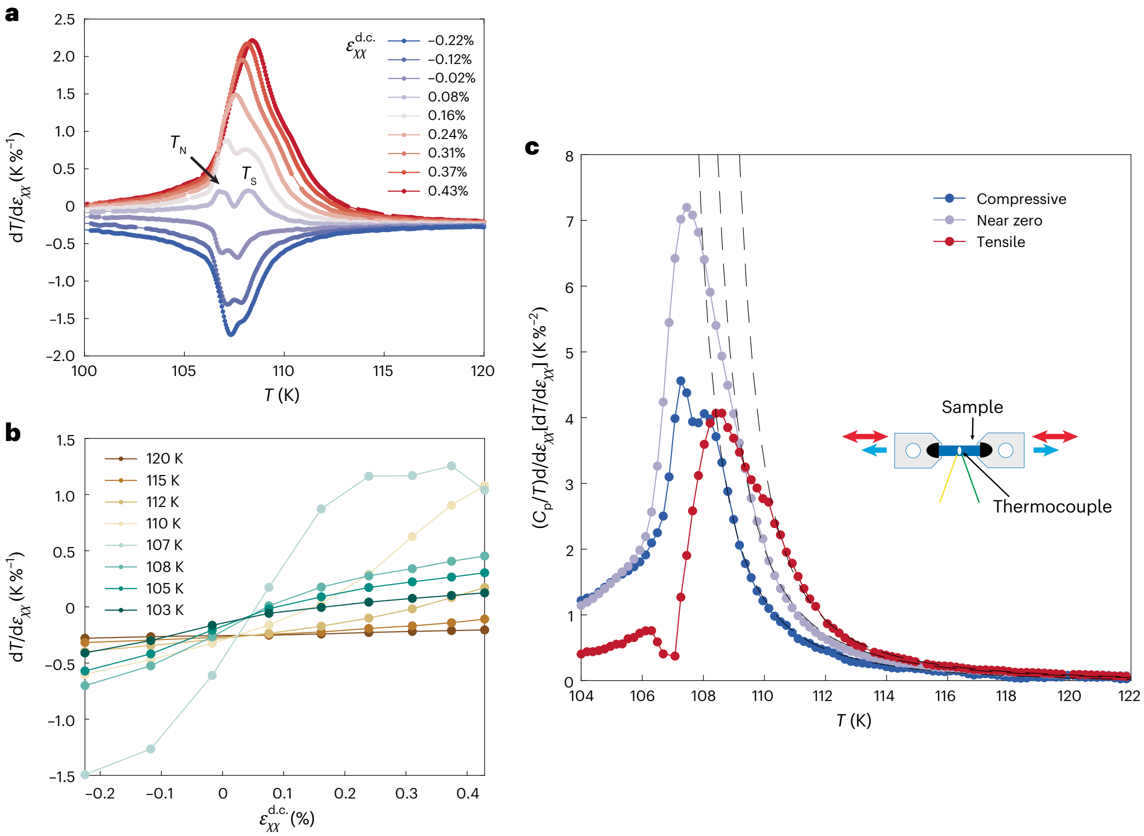

Fig. 5 | EC measurements of FePSe$_3$. **a**, Measured amplitude of temperature fluctuations divided by the amplitude of the estimated a.c. strain. The d.c. strains were induced at 123 K (denoted by the colour scheme; tensile is red and compressive is blue). The system was then cooled to 100 K. Zero strain was estimated by determining the d.c. strain where the minimum of the transition temperatures occurred and where the diverging EC signal changed concavity. T_N and T_S denote the signatures for the AFM and nematic phase transition, respectively. **b**, EC response binned at select temperatures and plotted versus the d.c. strain. The slope of the response versus strain for different strain regimes was extracted to determine the nematic 'susceptibilities', as plotted in **c**. **c**, Strain derivative of the normalized ECE, with the colours indicating what d.c.-strain regime the linear fit was performed in, namely, tensile (red), near-zero strain (purple) and compressive (blue). These quantities were determined by normalizing the data in **b** by the heat capacity background[35] divided by the temperature ratio. The black dashed lines denote the Curie–Weiss squared fits, with the parameters listed in Table 1.

temperature T_c, the ECE also produces a signal in proximity of the phase transition (regardless of the symmetry character of the phase transition):

$$\frac{dT}{d\varepsilon} = \frac{C^c_\varepsilon}{C^t_\varepsilon}\frac{dT_c}{d\varepsilon},$$

which is proportional to the ratio of the critical part of the heat capacity C^c_ε (the part shifted by strain along with T_c) to the total heat capacity of the sample C^t_ε, and the derivative of T_c with respect to strain[31]. Experimentally, EC measurements necessitate the sample to be mounted across a gap on a strain cell such that uniaxial stress is applied, which induces strain of both E_{2g} and A_{1g} characters that can—in theory—change the AFM phase transition temperature T_N for the case of FePSe$_3$.

In Fig. 5a, the quantity $dT/d\varepsilon_{xx}$ (approximated by dividing the amplitude of the temperature oscillations by the a.c. strain amplitude) is plotted, with the colour scheme indicating the d.c. offset strain estimated to be induced before cooling from 123 K (tensile in red and compressive in blue). Not only are nematic susceptibilities (marked by the high-temperature tail) present but heat capacity anomalies (marked by the bumps labelled T_S (nematic) and T_N (AFM)) are also present, which form the double-peak structure at temperatures close to the expected AFM phase transition. This can be interpreted as signatures of two separate phase transitions that evolve differently with d.c. strain: the higher-temperature one is a vestigial nematic transition marked by a peak with a corresponding susceptibility tail that broadens into a crossover as larger strains are applied, and the lower peak arises from the AFM transition[18]. As shown in Supplementary Information, both transition temperatures increase linearly for both compressive and tensile d.c. strains. This can be explained by the E_{2g} strain playing the dominant role in tuning the lower-temperature transition T_N followed by the higher-temperature transition T_S. This is because T_N is expected to be an even function of ε_{E2g} due to biquadratic coupling terms. The sign of the peak of the signal arising from the AFM heat capacity anomaly changes sign near the estimated zero strain, which corresponds to the sign switching of $dT_N/d\varepsilon_{xx}$. Furthermore, the diverging high-temperature tail changes sign as the d.c. strain changes, indicating that a nematic-susceptibility-like term proportional to the d.c. strain is being probed by this measurement.

Figure 5c displays the strain derivative of the normalized ECE, separately extracted in compressive-, near-zero- and tensile-strain regimes. This quantity is determined by measuring the corresponding slopes of the ECE signal versus d.c. strain (Fig. 5b) and normalizing them by the ratio of heat capacity to temperature. Although this quantity corresponds to the temperature derivative of the nematic susceptibility only in the zero-strain limit, it is still informative to fit to a Curie–Weiss squared form ($A/(T - T^*)^2$) in different strain conditions. The extracted 'susceptibilities' (Fig. 5c, black dashed lines) are quantitatively different between the compressive- and tensile-strain

Table 1 | Fitting parameters for the nematic susceptibilities from LD and EC measurements

Experiment	Strain range	Temperature range	A	T^*	C
LD, compressive	<−0.1%	>110 K	−14.7±6.9	106.3±2.2	−1.6±0.2
ECE, compressive	<−0.1%	>108.2 K	16.6±0.9	106.4±0.1	−0.05±0.01
ECE, near zero	>−0.1% and < 0.2%	>109 K	19.6±1.6	106.9±0.1	−0.04±0.02
ECE, tensile	>0.2% and < 0.4%	>110 K	17.6±1.6	107.7±0.1	−0.03±0.01

This table displays the ranges of strain and temperature in which the Curie–Weiss fit ($A/(T-T^*)+C$) was performed for the slope of the LD with respect to strain, as well the Curie–Weiss squared fits ($A/(T-T^*)^2+C$) for the temperature derivative of the susceptibilities extracted from the ECE.

regimes, with the Weiss temperatures ranging from 106.4 K to 107.7 K (Table 1). These temperatures agree well with the fitting from the LD measurements, corroborating the divergence of a nematic susceptibility from an optical and a thermodynamic measurement. Furthermore, the apparent asymmetry of the susceptibility-like quantities in the tensile- and compressive-strain regimes determined from the ECE measurements is not expected in an Ising system. This asymmetry is only prevalent in systems in which odd powers of the nematic order parameter are inherently present, like in the three-state Potts model, as more explicitly shown in Supplementary Information.

Our results establish $FePSe_3$ as an archetypal material system in which nematicity in a three-state Potts model can be studied. Using both optical and thermodynamic probes, we experimentally demonstrate that the nematic behaviour in such a model is distinct from that observed in typical tetragonal systems. In particular, the nature of the nematic fluctuations can be changed asymmetrically with strain. Finally, superconductivity has been reported to emerge in $FePSe_3$ as the AFM state is suppressed by pressure[34]. An interesting future direction is to investigate whether there is an intimate relationship between electronic nematicity and superconductivity in a three-state Potts system, similar to the relationship shown in Ising-nematic iron pnictides.

Online content

Any methods, additional references, Nature Portfolio reporting summaries, source data, extended data, supplementary information, acknowledgements, peer review information; details of author contributions and competing interests; and statements of data and code availability are available at https://doi.org/10.1038/s41567-024-02653-3.

References

1. Norman, M. R. The challenge of unconventional superconductivity. *Science* **332**, 196–200 (2011).
2. Monthoux, P., Pines, D. & Lonzarich, G. Superconductivity without phonons. *Nature* **450**, 1177–1183 (2007).
3. Malinowski, P. et al. Suppression of superconductivity by anisotropic strain near a nematic quantum critical point. *Nat. Phys.* **16**, 1189–1193 (2020).
4. Rubio-Verdú, C. et al. Moiré nematic phase in twisted double bilayer graphene. *Nat. Phys.* **18**, 196–202 (2022).
5. Chichinadze, D. V., Classen, L. & Chubukov, A. V. Nematic superconductivity in twisted bilayer graphene. *Phys. Rev. B* **101**, 224513 (2020).
6. Choi, Y. et al. Electronic correlations in twisted bilayer graphene near the magic angle. *Nat. Phys.* **15**, 1174–1180 (2019).
7. Jiang, Y. et al. Charge order and broken rotational symmetry in magic-angle twisted bilayer graphene. *Nature* **573**, 91–95 (2019).
8. Nie, L. et al. Charge-density-wave-driven electronic nematicity in a kagome superconductor. *Nature* **604**, 59–64 (2022).
9. Xu, Y. et al. Three-state nematicity and magneto-optical Kerr effect in the charge density waves in kagome superconductors. *Nat. Phys.* **18**, 1470–1475 (2022).
10. Jiang, Z. et al. Observation of electronic nematicity driven by the three-dimensional charge density wave in kagome lattice KV_3Sb_5. *Nano Lett.* **23**, 5625–5633 (2023).
11. Wu, P. et al. Unidirectional electron–phonon coupling in the nematic state of a kagome superconductor. *Nat. Phys.* **19**, 1143–1149 (2023).
12. Fernandes, R. M. & Venderbos, J. W. Nematicity with a twist: rotational symmetry breaking in a moiré superlattice. *Sci. Adv.* **6**, eaba8834 (2020).
13. Little, A. et al. Three-state nematicity in the triangular lattice antiferromagnet $Fe_{1/3}NbS_2$. *Nat. Mater.* **19**, 1062–1067 (2020).
14. Zhang, H. et al. Cavity-enhanced linear dichroism in a van der Waals antiferromagnet. *Nat. Photon.* **16**, 311–317 (2022).
15. Cui, J. et al. Chirality selective magnon-phonon hybridization and magnon-induced chiral phonons in a layered zigzag antiferromagnet. *Nat. Commun.* **14**, 3396 (2023).
16. Haglund, A. Thermal conductivity of MXY_3 magnetic layered trichalcogenides. PhD dissertation, Univ. of Tennessee (2019).
17. Ni, Z. et al. Signatures of Z_3 vestigial Potts-nematic order in van der Waals antiferromagnets. Preprint at https://arxiv.org/abs/2308.07249 (2023).
18. Fernandes, R. M., Orth, P. P. & Schmalian, J. Intertwined vestigial order in quantum materials: nematicity and beyond. *Annu. Rev. Condens. Matter Phys.* **10**, 133–154 (2019).
19. Fernandes, R., Chubukov, A. & Schmalian, J. What drives nematic order in iron-based superconductors? *Nat. Phys.* **10**, 97–104 (2014).
20. Zhang, Q. et al. Observation of giant optical linear dichroism in a zigzag antiferromagnet $FePS_3$. *Nano Lett.* **21**, 6938–6945 (2021).
21. Hwangbo, K. et al. Highly anisotropic excitons and multiple phonon bound states in a van der Waals antiferromagnetic insulator. *Nat. Nanotechnol.* **16**, 655–660 (2021).
22. Zhang, X.-X. et al. Spin dynamics slowdown near the antiferromagnetic critical point in atomically thin $FePS_3$. *Nano Lett.* **21**, 5045–5052 (2021).
23. Ni, Z. et al. Imaging the Néel vector switching in the monolayer antiferromagnet $MnPSe_3$ with strain-controlled Ising order. *Nat. Nanotechnol.* **16**, 782–787 (2021).
24. Ni, Z. et al. Direct imaging of antiferromagnetic domains and anomalous layer-dependent mirror symmetry breaking in atomically thin $MnPS_3$. *Phys. Rev. Lett.* **127**, 187201 (2021).
25. Chu, H. et al. Linear magnetoelectric phase in ultrathin $MnPS_3$ probed by optical second harmonic generation. *Phys. Rev. Lett.* **124**, 027601 (2020).
26. Schäfer, F. & Kleemann, W. High-precision refractive index measurements revealing order parameter fluctuations in $KMnF_3$ and NiO. *J. Appl. Phys.* **57**, 2606–2612 (1985).
27. Gehring, G. On the observation of critical indices of primary and secondary order parameters using birefringence. *J. Phys. C* **10**, 531 (1977).
28. Ferré, J. & Gehring, G. Linear optical birefringence of magnetic crystals. *Rep. Prog. Phys.* **47**, 513 (1984).

29. Wiedenmann, A., Rossat-Mignod, J., Louisy, A., Brec, R. & Rouxel, J. Neutron diffraction study of the layered compounds $MnPSe_3$ and $FePSe_3$. *Solid State Commun.* **40**, 1067–1072 (1981).
30. Cenker, J. et al. Reversible strain-induced magnetic phase transition in a van der Waals magnet. *Nat. Nanotechnol.* **17**, 256–261 (2022).
31. Chu, J.-H., Kuo, H.-H., Analytis, J. G. & Fisher, I. R. Divergent nematic susceptibility in an iron arsenide superconductor. *Science* **337**, 710–712 (2012).
32. Ikeda, M. S. et al. AC elastocaloric effect as a probe for thermodynamic signatures of continuous phase transitions. *Rev. Sci. Instrum.* **90**, 083902 (2019).
33. Ikeda, M. S. et al. Elastocaloric signature of nematic fluctuations. *Proc. Natl Acad. Sci. USA* **118**, e2105911118 (2021).
34. Wang, Y. et al. Emergent superconductivity in an iron-based honeycomb lattice initiated by pressure-driven spin-crossover. *Nat. Commun.* **9**, 1914 (2018).
35. Bhutani, A., Zuo, J. L., McAuliffe, R. D., dela Cruz, C. R. & Shoemaker, D. P. Strong anisotropy in the mixed antiferromagnetic system $Mn_{1-x}Fe_xPSe_3$. *Phys. Rev. Mater.* **4**, 034411 (2020).

Methods

Crystal growth

Single crystals of $FePSe_3$ were synthesized by the chemical vapour transport method using iodine as the transport agent. Stoichiometric amounts of iron powder (99.998%), phosphorus powder (98.9%) and selenium powder (99.999%) were mixed with iodine (~1 mg cm^{-3}) and sealed in quartz tubes (~10 cm in length) under a high vacuum. The tubes were placed in a horizontal two-zone furnace. Large and thin crystals (~10 × 10 × 0.01 mm^3) of $FePSe_3$ were then obtained after quickly heating the precursor up to 800 °C for the source end and 750 °C for the sink end, dwelling for 12 h and quickly cooling down to room temperature.

Strain measurements and strain calibration

To deterministically apply strain along certain directions of the Fe honeycomb lattice, we first exfoliated the flakes onto polydimethylsiloxane slabs. We found $FePSe_3$ flakes to have a distinctive cleavage direction when exfoliated onto substrates, as is the case with many other van der Waals materials[36], which allowed us to infer the zigzag/armchair direction of the material from the sample images. The flakes were then transferred onto thin silicon rectangles that were adhered to two-dimensional flexure sample plates produced by Razorbill Instruments using STYCAST 2850 FT epoxy with the identified crystal axes carefully aligned to the strain direction. Extended Data Fig. 2 shows an optical image of the prepared strain sample. Strain measurements were conducted using homebuilt strain cells[30]. The strength of the applied strain to the sample was measured by tracking the Raman shift in a silicon phonon peak (centred at ~525 cm^{-1}) as a function of the piezo-voltage (Extended Data Fig. 3). The Raman shift was then converted into a strain value by using the previously reported strain shift rate. A previous study[30] indicated that the strain shift rate of the silicon phonon mode is an accurate measure of the applied strain to the sample. The presented strain values have been shifted to account for the built-in strain from sample preparation and thermal expansion coefficient mismatch in the strain system. The built-in strain was identified through the domain population modelling of the LD response of the sample at the base temperature. This study was conducted using a cold-finger cryostat from Montana Instruments. Due to the large thermal load introduced by the cryo-strainer, there is a thermal shift for the strain samples with respect to the non-strained sample presented. We have corrected for this thermal offset in the measurements presented for the strained sample. The offset was identified by measuring a non-strained $FePSe_3$ sample in the same measurement scheme and noting the shift in the transition temperature (Extended Data Fig. 3).

LD spectroscopy

The measurements were carried out in the reflection geometry. A 633 nm He–Ne laser was doubly modulated by a photoelastic modulator with a retardance of $\lambda/2$ and a mechanical chopper. After phase modulation, the light passed through a half-wave plate and then was focused down onto the sample at normal incidence with an objective lens. A laser power of ~5 μW was used. The reflected light was detected by a photodiode and demodulated at 100 kHz and 1 kHz, which corresponds to the photoelastic modulator linear polarization modulation frequency and the chopper modulation frequency, respectively. We also conducted LD spectrum measurements using a supercontinuum laser and a tuneable filter set with 1 nm spectral resolution. We observed a broad LD response centred at about 620 nm (Extended Data Fig. 1). The broad response allows the 633 nm laser to provide suitable excitation energy for the measurements. LD reading from the sample at 295 K was subtracted from the presented data to remove background anisotropy introduced by the optical components (Extended Data Fig. 7). The LD measurement probes the nematic order parameter (**n**), which is expressed in terms of the magnetic order parameters (L_i, where $i = 1$, 2 and 3, corresponding to each choice of the zigzag AFM order)[13]:

$$\mathbf{n} = (n_1, n_2) \propto \left(|L_1|^2 + |L_2|^2 - 2|L_3|^2, \sqrt{3}|L_1|^2 - \sqrt{3}|L_2|^2\right).$$

Domain population model of LD signal

The LD signals of the two individual domains are described by $\cos(2\theta)$ and $\cos(2(\theta + 2\pi/3))$. The total LD signal is then a mixture of the two domains:

$$\mathrm{LD}\,(\theta) = f(\varepsilon)\cos\,(2\theta) + [1 - f(\varepsilon)]\,\cos(2(\theta + 2\pi/3)),$$

where $f(\varepsilon)$ represents the strain-dependent proportion of each nematic director swept from 0 to 1. Extended Data Fig. 8 shows the excellent agreement of the experimental results shown in Fig. 2a to this model. To explain the trend observed in Fig. 2b, we included the third nematic domain with an angle of $-2\pi/3$ in the domain population model. The overall LD signal is expressed as

$$\mathrm{LD}\,(\theta) = f(\varepsilon)\cos\,(2\theta) + \left(\frac{1}{2}\right)[1 - f(\varepsilon)]\cos\left(2\left(\theta + \tfrac{2\pi}{3}\right)\right) + \left(\frac{1}{2}\right)[1 - f(\varepsilon)]\cos\left(2\left(\theta - \tfrac{2\pi}{3}\right)\right).$$

As shown by the schematic in Fig. 2f, this model describes a situation in which the nematic domains described by $\cos(2(\theta + 2\pi/3))$ and $\cos(2(\theta - 2\pi/3))$ are degenerate and equally populated as tensile strain is applied. Similarly, using this domain population model, we accurately obtain the trend observed in Fig. 2b. Under compressive strain, the zigzag spin chain aligns parallel to the strain direction as the bond distance between Fe–Fe atoms distinctly becomes the shortest. This strain-induced anisotropy relieves the degeneracy between the three nematic directors, and the zigzag nematic chain aligns along the shortest Fe–Fe bonds. Under tensile strain, rather than having a clear direction of Fe–Fe bonds that are the shortest, two chains of Fe–Fe bonds (rotated by $2\pi/3$ between each other) are equivalent. These two zigzag chains remain energetically degenerate, and the LD response becomes a mixture of these two domains.

Raman measurement

A He–Ne laser (633 nm) was used to excite the $FePSe_3$ sample, which was placed in a closed-cycle cryostat with temperature ranging from 5 K to 300 K. The Raman measurements were polarization resolved and collected by a spectrometer with a liquid-nitrogen-cooled charge-coupled device camera (Extended Data Figs. 5 and 6).

EC measurements

For the EC measurements, a commercial Razorbill CS100 strain cell was used to induce strain to the samples, which were cut 90° from the crystal facets to be approximately 1 mm × 0.4 mm × 0.02 mm in size. The samples were secured between two sets of mounting plates using STYCAST 2850 FT epoxy, which were screwed into the strain cell, to have a gap of approximately 0.7 mm. An a.c. voltage of 5 V root mean squared at 14 Hz was applied to the outer piezoelectric stacks of the strain cell, which corresponded to applying an a.c. displacement of the sample of approximately 0.01% of its length. This frequency was experimentally determined by measuring the EC signal at 120 K for frequencies in the range of 5–50 Hz and choosing the frequency with the largest response. This implied that the frequency was at the plateau of the relevant thermal transfer function, which did not observably shift in the temperature range measured. The d.c. voltages were applied to the inner piezoelectric to reach a strain range of 0.7%. To approximate the strain that the sample experienced, the capacitance of the displacement sensor built into the strain cell was measured, which provided the relative displacement of the sample plates; the obtained value was then divided by the length of the gap. This, however, only approximated ε_{xx} of the sample as it assumes 100% strain transmission.

The temperature fluctuations in the sample induced by the a.c. strain were measured using a home-made type E (chromel–constantan) thermocouple. The chromel and constantan wires (50 µm diameter) were thermally anchored to an outer part of the strain cell and silver pasted together to the sample (Fig. 5c, inset). The voltage between the two wires was measured with an SR860 lock-in amplifier at the frequency of the strain being applied to obtain the amplitude of the temperature fluctuations.

Data availability

The datasets generated during and/or analysed during this study are available from the corresponding authors upon reasonable request. Source data are provided with this paper.

References

36. Guo, Y. et al. Distinctive in-plane cleavage behaviors of two-dimensional layered materials. *ACS Nano* **10**, 8980–8988 (2016).

Acknowledgements

We thank Q. Zhang for substantial insights. This work was mainly supported by the Department of Energy, Basic Energy Sciences, Materials Sciences and Engineering Division (DE-SC0012509). Strain devices were partially supported by the Air Force Office of Scientific Research (AFOSR) Multidisciplinary University Research Initiative (MURI) program, grant no. FA9550-19-1-0390. Bulk crystal growth and EC measurements were supported by NSF MRSEC DMR-2308979 and the Gordon and Betty Moore Foundation's EPiQS Initiative, grant no. GBMF6759 (to J.-H.C.). We also acknowledge the use of facilities and instrumentation supported by NSF MRSEC DMR-1719797. X.X. and J.-H.C. acknowledge support from the State of Washington-funded Clean Energy Institute.

Author contributions

X.X., K.H., J.-H.C., H.W. and E.R. conceived the experiment. K.H fabricated the samples and performed the optical measurements. J.C. designed and built the strain cell for atomically thin flakes. E.R. performed the EC measurement, and Q.J. synthesized and characterized the bulk crystals under the supervision of J.-H.C. D.X. constructed the domain population model. All authors contributed to the data analysis and interpretation. K.H., X.X., E.R. and J.-H.C. wrote the paper with input from all authors. All authors discussed the results and commented on the paper.

Competing interests

The authors declare no competing interests.

Additional information

Extended data is available for this paper at https://doi.org/10.1038/s41567-024-02653-3.

Supplementary information The online version contains supplementary material available at https://doi.org/10.1038/s41567-024-02653-3.

Correspondence and requests for materials should be addressed to Jiun-Haw Chu or Xiaodong Xu.

Peer review information *Nature Physics* thanks Deep Jariwala, Gediminas Simutis and the other, anonymous, reviewer(s) for their contribution to the peer review of this work.

Reprints and permissions information is available at www.nature.com/reprints.

https://doi.org/10.1038/s41567-024-02653-3

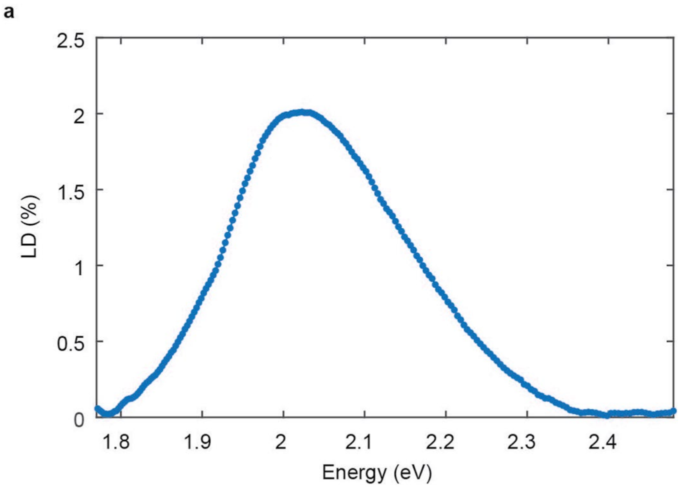

Extended Data Fig. 1 | Linear dichroism spectrum. Linear dichroism signal as a function of incident photon energy for a thin-bulk $FePSe_3$ sample at 5 K. The spectrum shows a broad LD response centered around 2 eV. The photon energy dependent LD response is possibly due to a resonance effect with a *d*-*d* electronic transition. Previous measurements on $FePS_3$ showed similar enhancement of LD response at known *d*-*d* transitions.

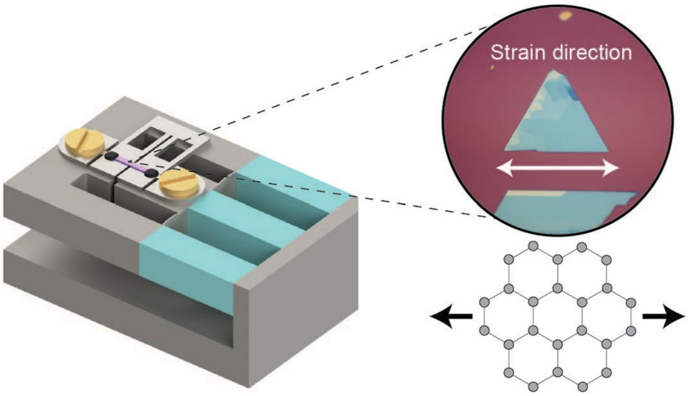

Extended Data Fig. 2 | Strain apparatus and crystal response to strain. Schematic of the strain cell used for the strain measurements and optical image of a representative strain sample. The crystal zigzag direction was aligned along the strain direction.

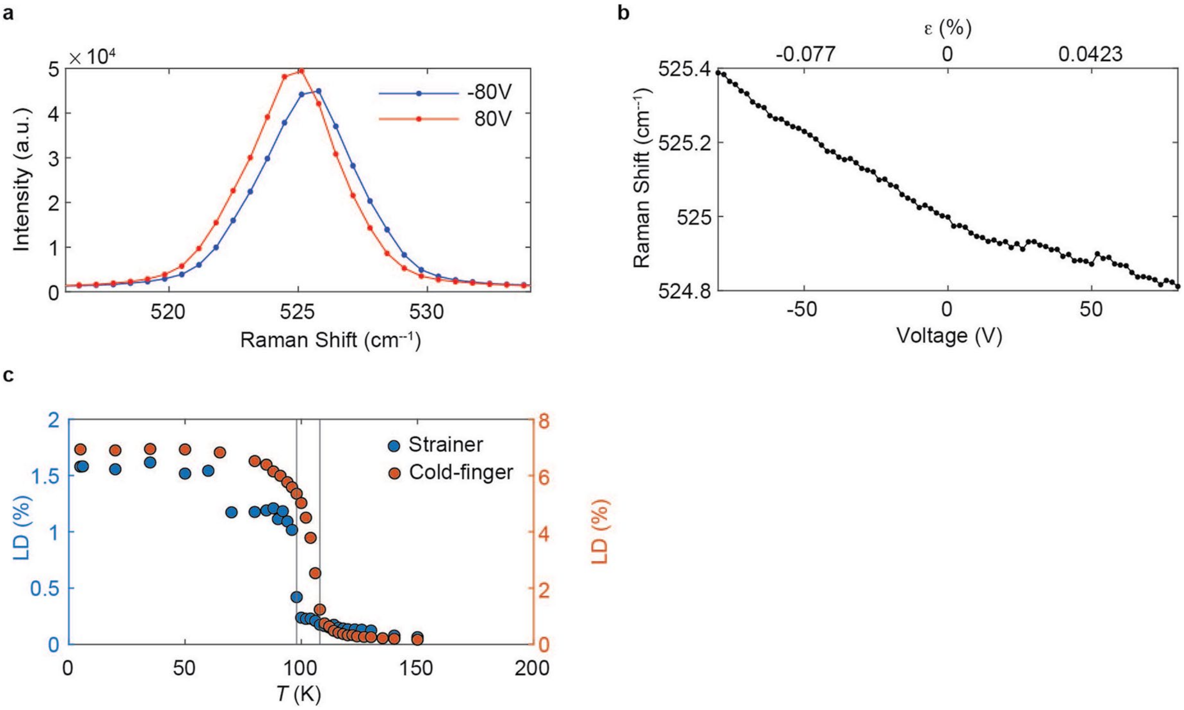

Extended Data Fig. 3 | Strain calibration using Si phonon mode and Thermal calibration. **a**, Raman spectra of the silicon Raman mode centered around 525 cm^{-1} with −80 V (blue) and 80 V (red) applied to the strain cell. **b**, Raman shift of the silicon Raman mode as a function of the piezo voltage. **c**, Linear dichroism versus temperature for a non-strained, thin bulk FePSe$_3$ flake on the strainer setup, showing the shift (~10 K) in the transition temperature due to the increased thermal load of the strainer. The x-axis shows the nominal thermocouple reading.

https://doi.org/10.1038/s41567-024-02653-3

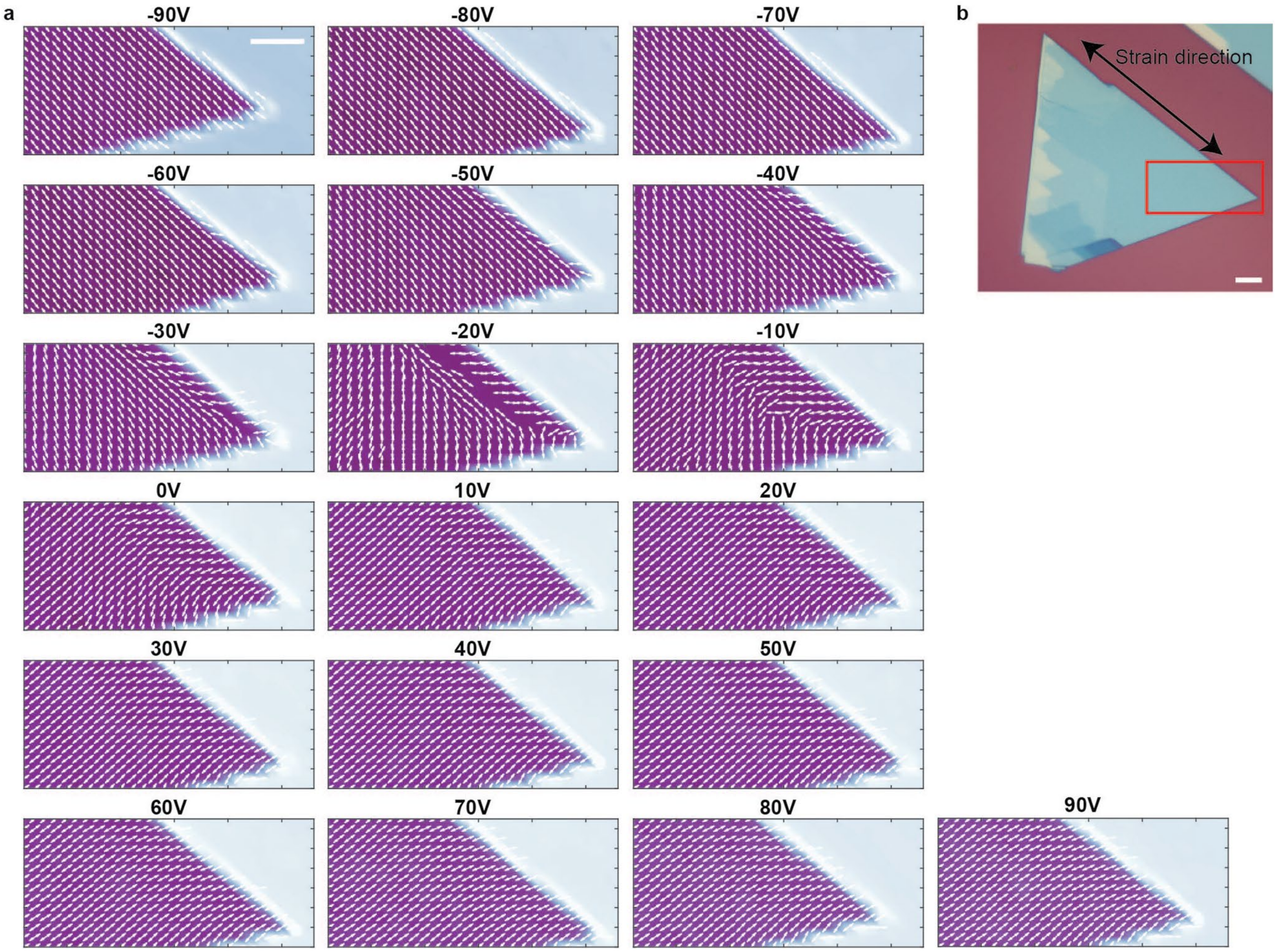

Extended Data Fig. 4 | Linear dichroism spatial mapping. **a**, Nematic directors (represented by the white arrows) at each sampled point overlaid on top of the reflection raster map for various piezo voltages. The raster map was scanned over 28 $\mu m \times 14$ μm area with 1 μm step sizes. The maximally negative voltage corresponds to the highest compressive strain applied. Scale bar: 5 μm. The absence of distinct nematic domains, which are separated by $2\pi/3$, across the sample demonstrates that the results of Fig. 2a, b are not a product of our probe beam concomitantly sampling adjacent nematic domains. **b**, Optical image of the measured strain sample. The red box represents the area which the LD mapping was measured, and the black arrow shows the strain direction. Scale bar: 5 µm.

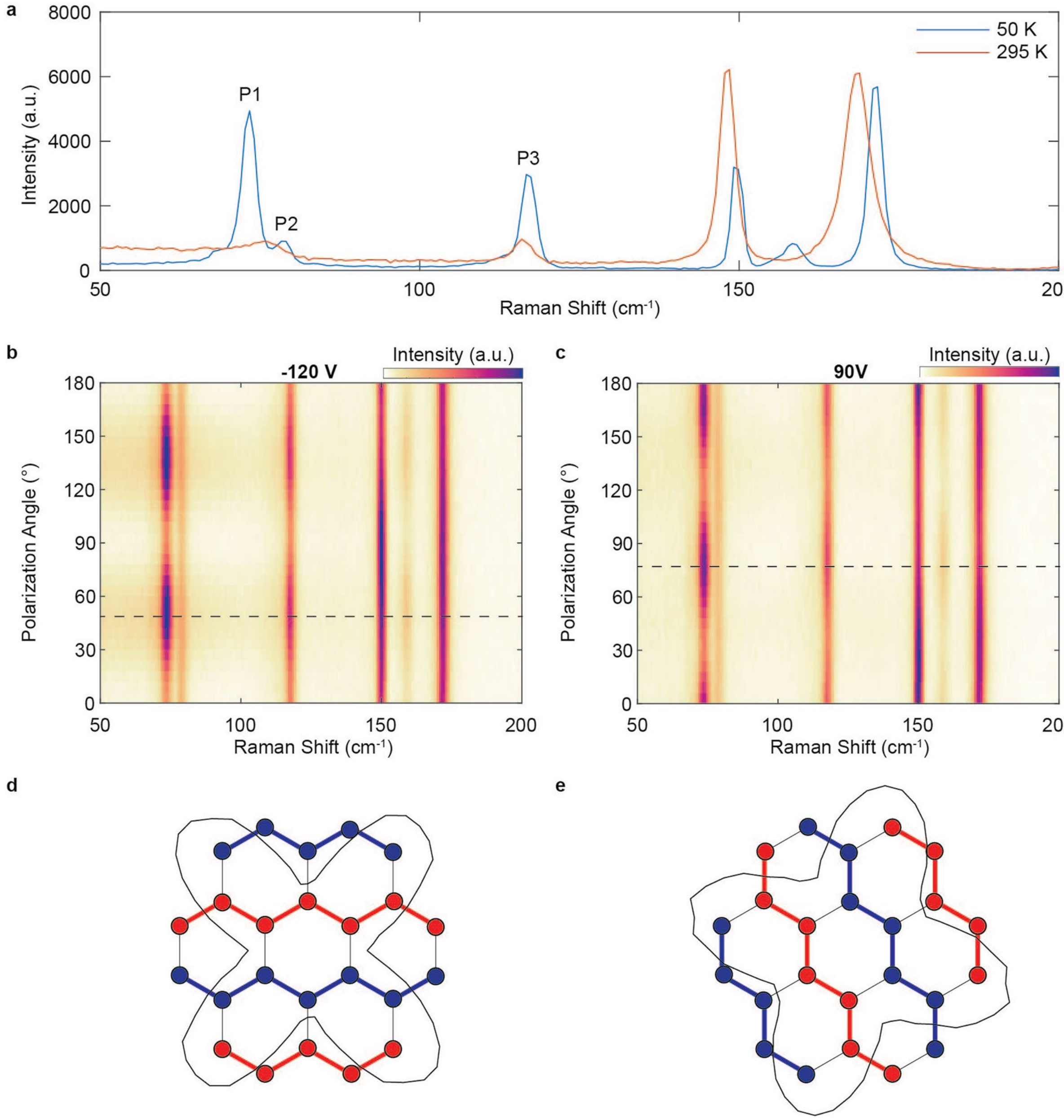

Extended Data Fig. 5 | Polarization-resolved Raman spectroscopy of the strain FePSe$_3$ sample. a, Raman response of a thin-bulk flake at two thermal points. Labelled peaks (P1, P2, and P3) correspond to Raman modes associated with the zigzag AFM order. **b, c**, Co-linearly polarized Raman scattering as the incident polarization is rotated for compressive (−120 V) and tensile (90 V) strain, respectively. **d, e**, Polar plot of the integrated intensity of the Raman mode labelled P1 superimposed onto zigzag orders at compressive **(d)** and tensile **(e)** strain. P1 Raman mode exhibits a four-fold symmetry that is rotationally separated by $\pi/4$ with respect to the zigzag order. Thus, a $2\pi/3$-shift in the zigzag order would result in a $\pi/6$-shift in the incident polarization dependence of the Raman mode.

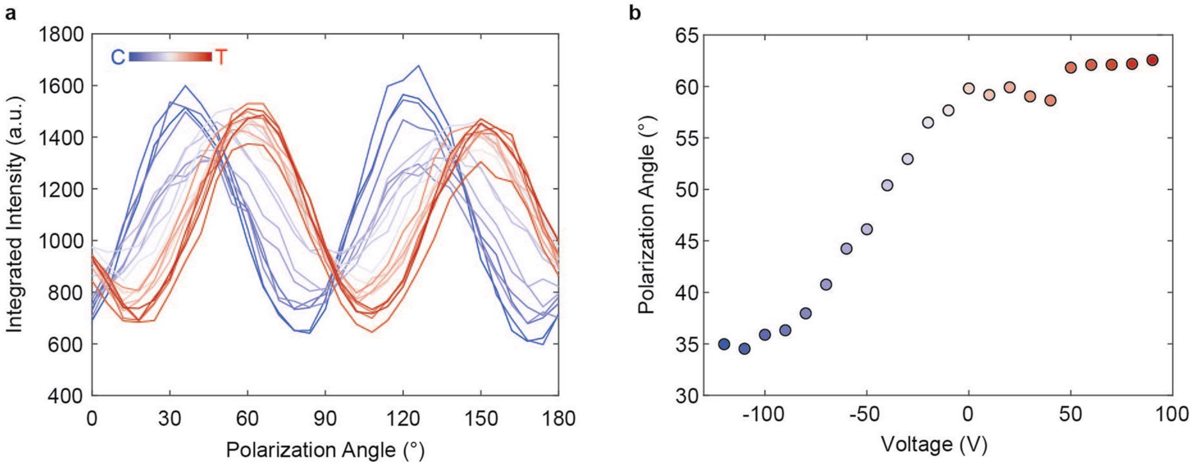

Extended Data Fig. 6 | Polarization-dependent intensity of Raman mode at ~73 cm^{-1}. **a**, Polarization dependence of the integrated intensity of Raman mode labelled P1 in Extended Data Fig. 5 as strain is swept from compressive (blue curves) to tensile (red curves) side. **b**, Incident polarization angle values where the Raman peak reaches the maximum value. There is near 30-degree rotation as strain is swept from compressive to tensile strain.

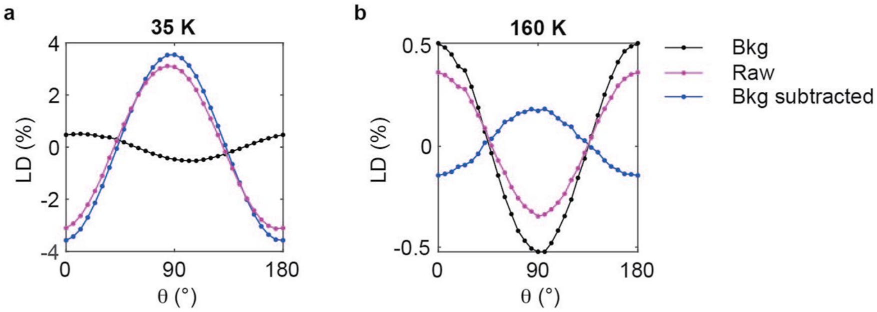

Extended Data Fig. 7 | Raw data and background subtraction. **a,b**, Polarization-dependent LD responses at 35 K and 160 K, respectively. The black curves represent the background LD response from the sample at 295 K. The pink curves represent the raw LD response observed from the sample. The blue curves are the LD response after subtracting the background response from the raw data.

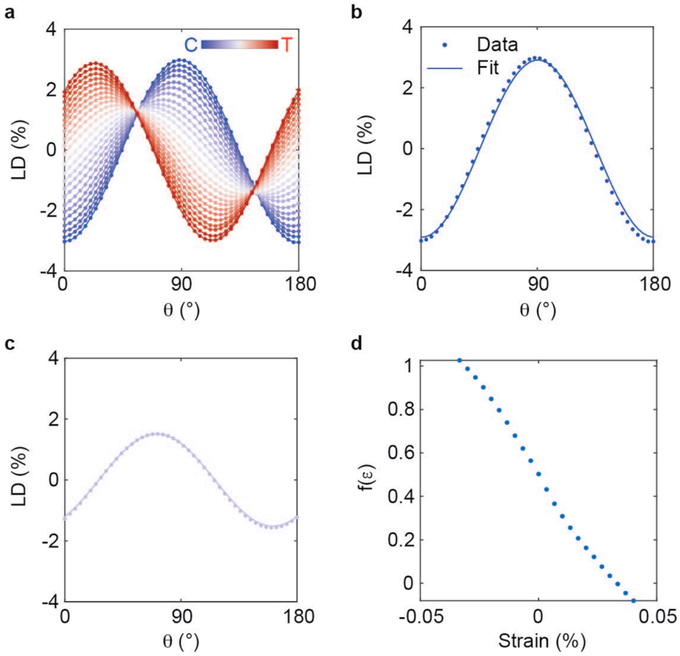

Extended Data Fig. 8 | Domain Population Model Fitting. a, Polarization-dependent LD response shown in Fig. 2a. **b,c**, LD responses and corresponding fit to function, $LD(\theta) = f(\varepsilon)\ \cos(2\theta) + [1 - f(\varepsilon)]\cos(2(\theta + 2\pi/3))$, to extract $f(\varepsilon)$ at −0.033% and 0% strain, respectively. **d**, $f(\varepsilon)$ versus strain for LD response shown in Fig. 2a.